6

Regularized Inversion for Towed-Array Shape Estimation

Stan E. Dosso
Nicole E. Collison

ABSTRACT This chapter describes a new approach to the inverse problem of estimating the shape of a ship-towed hydrophone array using near-field acoustic measurements. The data consist of the relative travel times of arrivals along direct and reflected paths from sources deployed by two consort ships maintaining station with the moving tow ship (the "dual-shot method"). Previous inversion algorithms typically apply least-squares methods based on simplifying assumptions, such as straight-line propagation and exact knowledge of the source positions. Here, a regularized inversion is developed based on ray theory, with the source positions included as unknown parameters subject to a priori estimates and uncertainties. In addition, a minimum-structure array shape is determined by minimizing the three-dimensional curvature subject to fitting the data to a statistically meaningful level, thereby reducing spurious fluctuations (roughness) in the solution. Finally, the effect of the survey geometry is investigated by defining a mean sensor-position error measure based on the a posteriori uncertainty of the inversion. The optimal source configuration is determined by minimizing this error with respect to the source positions using an efficient hybrid optimization algorithm. The inversion and optimization procedures are illustrated using realistic synthetic examples.

6.1 Introduction

Towed arrays consist of a line of hydrophones housed in a neutrally buoyant, acoustically transparent hose, and are commonly used in military sonar systems and marine seismic exploration. For optimal array-processing performance, it is important to determine the relative positions of the sensors (or, equivalently, the shape of the array), a problem commonly referred to as array element localization (AEL). For example, a general rule to achieve a loss of less than 1 dB in array-processing gain requires the sensor positions be known to within $\lambda/10$, where λ is the wavelength at the frequency of interest [H+96]. The shape of a towed array is dynamic, and is influenced by changes in the tow ship's course and speed and by shear currents in the water column. Array-mounted instruments, such as depth and heading sensors, can provide information on array shape. Typically, such instruments are distributed at intervals along the array, and do not provide measurements of the positions of individual sensors. Sensor locations can be ob-

tained by smoothly interpolating between measured positions (e.g., employing a cubic spline), or by applying hydrodynamic modeling which attempts to account for the dynamic behavior of an array with known properties (weight, drag, etc.) under towing conditions.

Van Ballegooijen et al. [vB+89] introduced an acoustic approach to towed-array shape estimation which does provides individual sensor positions. This method can be used to independently verify array shapes derived from depth and heading measurements, or can be applied in conjunction with these measurements (it is not, however, a practical approach for all operational scenarios). The approach, known as the "dual-shot method," makes use of explosive sources deployed in the water column by two consort ships maintaining station with the moving tow ship. The suggested survey configuration is to have the consort ships 500–1000 m away from the array and spaced at an angle of 90° relative to the array center. The measured data ideally consist of relative travel times of the acoustic arrivals along direct, bottom-reflected, and bottom–surface reflected paths; however, in practical cases, one or other of the reflected arrivals may not be usable. Assuming the source positions and ocean sound speed are known, the travel-time data can be inverted to infer the positions of the array sensors. A reference hydrophone installed on the tow ship serves to locate the array with respect to the ship. The source depths should be approximately equal to the array depth, and the survey is ideally carried out at a deep-water site with a flat bottom. This ensures that the direct arrivals travel horizontally while the reflected arrivals travel nearly vertically. This survey geometry is designed to provide good three-dimensional (3-D) sensor localization, with the direct-path arrivals providing horizontal (x–y) control, and the reflected arrivals providing vertical (z) control.

The acoustic inversion applied to the dual-shot method [vB+89] represents an application of the least-squares method (minimizing the squared data error). Other approaches to similar AEL inversion problems are described in [H+96], [CD82], [Mil83], [SH90], [B+96], and [OC97]. This chapter develops a new approach for towed-array shape estimation. The algorithms presented here represent an extension of the approach to AEL recently developed for moored horizontal and vertical hydrophone arrays in [D+98b], [D+98a], and [DS99]. A number of sources of error, neglected in most previous AEL inversions, are addressed in the algorithms developed here. For instance, AEL inversion algorithms typically treat the source positions as known parameters. However, the inevitable errors in source positions are often nonnegligible, and in some cases cause larger inversion errors than the uncertainties of the travel-time data (i.e., source-position errors can represent the limiting factor in AEL inversion). Therefore, the source locations are not treated as known quantities here, but rather are included as unknown parameters (subject to a priori estimates with uncertainties) in the inversion algorithm. Another source of error often neglected involves the curvature of acoustic ray paths due to the depth-dependence of the ocean sound-speed profile. To address this, a general raytracing-based inversion algorithm is developed here. Third, errors in the measured sound-speed profile affect the accuracy of AEL inversion. Sound-speed measurements are generally accurate in a relative sense, but can suffer from bias

errors of up to 2 m/s due to inaccurate calibration [VH98]. Hence, the sound-speed bias is also included as a (constrained) unknown in the inversion. It should be noted that it is also possible for the ocean sound speed to vary both laterally and temporally in an unknown manner during an AEL survey; however, these uncertainties are not constrained by the acoustic data and will not be considered here.

The inversion algorithm is formulated to include both the travel-time data and available a priori information. In addition to prior estimates for some parameters (source positions, sound-speed bias), the a priori information also includes the physical expectation that the array shape is essentially smooth (i.e., does not involve small-scale roughness or fluctuations). This is applied by minimizing the three-dimensional curvature (roughness) of the array, subject to fitting the data to a statistically meaningful level, to obtain a minimum-structure solution. This essentially applies a priori information about the correlation between sensor positions, rather than information about the positions themselves. Minimizing the array curvature, subject to fitting the data, is physically reasonable, since the effect of towing the array (even while turning) and the stiffness of the array-housing tube typically preclude excessive roughness (e.g., sharp zig-zags in array shapes). In addition, this procedure produces the simplest array shape that is consistent with the data. Any deviations from a straight array are definitely required by the data, and are not artifacts of the inversion algorithm. Seeking minimum-structure solutions is philosophically consistent with Occam's Razor, and in geophysical inversion is often referred to as Occam's inversion [C+87]. In contrast, the least-squares method typically over-fits the data, in effect fitting the noise as well as the data, which can lead to unphysically rough solutions that complicate acoustic signal analysis.

A final issue concerns the use of relative travel-time measurements in AEL inversion. Two approaches are possible here. The first approach is to remove the source instants from the problem by considering appropriate differences between the relative travel times as the data to be inverted. The alternative is to treat the relative travel times as the data, and include each source instant as an unknown parameter to be determined in the inversion. The latter approach is adopted here since it results in data with smaller uncertainties, and since it allows the inversion algorithm greater scope in the application of a priori information.

AEL represents a nonlinear inverse problem that is inherently nonunique, and a closed-form solution does not exist. An effective approach is based on local linearization and iteration, reducing the nonlinear problem to a series of linear inversions that can be solved using methods of linear inverse theory. Section 6.2.1 considers linearization of the AEL inversion, and Secction 6.2.2 describes linearized inversion with application of a priori information via the method of regularization. In addition to determining the source positions, an estimate of the error in these positions is derived. These error estimates can be applied to the problem of designing optimal AEL surveys by minimizing the sensor-position error with respect to the source positions, as described in Section 6.2.3. The ray-theory basis for the inversion and optimization algorithms is outlined in Section 6.2.4.

In Section 6.3, the array-shape inversion and optimal survey design are illustrated with a series of synthetic examples.

6.2 Theory

6.2.1 *Linearization*

The set of N acoustic arrival times $\mathbf{t}$ measured in an AEL survey can be written in general vector form as

$$\mathbf{t} = \mathbf{T}(\mathbf{m}) + \mathbf{n}. \tag{6.1}$$

In (6.1), the forward mapping $\mathbf{T}$ represents the arrival times of the acoustic signals along ray paths between sources and receivers (an explicit expression for $\mathbf{T}$ and an efficient method of computing ray arrival times is given in Section 6.2.4). The model $\mathbf{m}$ of M unknown parameters consists of three-dimensional position variables x_i, y_i, z_i for each sensor, position variables x_j, y_j, z_j and source instant t_j^0 for each source, and the sound-speed bias c_b. Finally, $\mathbf{n}$ represents the data errors (noise). Equation (6.1) defines the AEL inverse problem: given a dataset of measured arrival times $\mathbf{t}$ and knowledge of the forward mapping $\mathbf{T}$, determine the model parameters $\mathbf{m}$ which gave rise to the data. As mentioned previously, this inverse problem is nonlinear; however, a local linearization is obtained by expanding $\mathbf{T}(\mathbf{m}) = \mathbf{T}(\mathbf{m_0} + \delta\mathbf{m})$ in a Taylor series to first order about an arbitrary starting model $\mathbf{m_0}$ to yield

$$\mathbf{t} = \mathbf{T}(\mathbf{m_0}) + \mathbf{J}\delta\mathbf{m}, \tag{6.2}$$

where $\delta\mathbf{m}$ represents an unknown model perturbation and $\mathbf{J}$ is the Jacobian matrix consisting of the partial derivatives of the data functionals with respect to the model parameters

$$J_{kl} = \partial T_k(\mathbf{m_0})/\partial m_l \tag{6.3}$$

(partial derivatives of the ray travel time are derived in Section 6.2.4). Defining $\delta\mathbf{t} = \mathbf{t} - \mathbf{T}(\mathbf{m_0})$, the expansion can be written

$$\mathbf{J}\delta\mathbf{m} = \delta\mathbf{t}. \tag{6.4}$$

Equation (6.4) defines a linear inverse problem for $\delta\mathbf{m}$ which can be solved using methods of linear inverse theory. Once $\delta\mathbf{m}$ is determined, the corresponding model solution is $\mathbf{m} = \mathbf{m_0} + \delta\mathbf{m}$. Since nonlinear terms are neglected in (6.4), the model $\mathbf{m}$ may not adequately reproduce the measured data. In this case, the starting model is updated, $\mathbf{m_0} \leftarrow \mathbf{m}$, and the inversion is repeated iteratively until an acceptable solution is obtained.

Least-squares methods are typically applied to invert (6.4), provided the inversion is well-posed. For ill-conditioned inversions, some form of minimum-norm solution is usually applied (i.e., the perturbation $|\delta\mathbf{m}|^2$ is minimized at each iteration), such as singular value decomposition [CD82] or Levenberg–Marquardt

[Mil83], [OC97] inversion. This approach has been referred to as the "creeping" method [S+90] since it iteratively progresses toward a solution by a series of small perturbations, with the final model retaining a dependence on the initial starting model. Note that since the linear inverse problem (6.4) is formulated in terms of the model perturbation (not the model), a priori information about the model cannot be included directly in the inversion.

An alternative to the creeping method can be formulated by substituting $\delta\mathbf{m} = \mathbf{m} - \mathbf{m}_0$ into expansion (6.4) to obtain [Old83]:

$$\mathbf{J}\mathbf{m} = \delta\mathbf{t} + \mathbf{J}\mathbf{m}_0 \equiv \mathbf{d}. \tag{6.5}$$

This expression relates known quantities (the right side, which may be considered modified data $\mathbf{d}$) directly to $\mathbf{m}$: the linearized inverse problem is formulated in terms of the model, not the model perturbation. In this case, a priori information regarding the model can be applied directly to the inversion, often leading to a more physically meaningful solution [Old83]. This approach has been referred to as the "jumping" method [S+90], since the size of the model change at each iteration is not minimized and the final solution is generally independent of the starting model. The jumping method was first applied to AEL inversion in [D+98a] and [D+98b]; this approach is also followed here.

6.2.2 *Regularized Inversion*

To consider the linear inverse problem (6.5), assume that the error n_i on datum t_i is due to an independent, Gaussian distributed random process with zero mean and standard deviation ν_i. The least-squares solution for a system of linear equations (6.5) is found by minimizing the χ^2 misfit

$$\chi^2 = |\mathbf{G}(\mathbf{J}\mathbf{m} - \mathbf{d})|^2 \tag{6.6}$$

with respect to the model $\mathbf{m}$, where $\mathbf{G} = \mathrm{diag}[1/\nu_1, \ldots, 1/\nu_N]$ weights the data according to their uncertainties. The solution, determined by setting $\partial\chi^2/\partial\mathbf{m} = 0$, is

$$\mathbf{m} = \left[\mathbf{J}^T\mathbf{G}^T\mathbf{G}\mathbf{J}\right]^{-1}\mathbf{J}^T\mathbf{G}^T\mathbf{G}\mathbf{d}. \tag{6.7}$$

The least-squares approach provides an unbiased solution, provided the matrix to be inverted is nonsingular. In addition to the possibility of singularity, the matrix can be ill-conditioned, leading to an unstable inversion (small errors on the data lead to large errors on the solution). Ill-posed (singular or ill-conditioned) inverse problems result when the data do not contain enough linearly independent information to fully constrain the solution. In AEL, the source–receiver geometry essentially determines the conditioning of the inverse problem. Including the source positions, as well as the sensor positions, as unknowns always leads to an ill-posed inversion.

The method of regularization provides a particularly useful approach to ill-posed linear inversions. Regularization is based on formulating a unique, stable inversion by explicitly including a priori information regarding the solution. This

is accomplished by minimizing an objective function ϕ which combines a term representing the χ^2 data misfit and a regularizing term that imposes the a priori expectation that the model $\mathbf{m}$ in some manner resembles a prior estimate $\hat{\mathbf{m}}$:

$$\phi = |\mathbf{G}(\mathbf{Jm} - \mathbf{d})|^2 + \mu|\mathbf{H}(\mathbf{m} - \hat{\mathbf{m}})|^2. \tag{6.8}$$

In (6.8), $\mathbf{H}$ is a weighting matrix known as the regularization matrix (described below), and the variable μ serves as a trade-off parameter controlling the relative importance assigned to the data misfit and the a priori expectation in the minimization. The regularized solution is obtained by minimizing ϕ with respect to $\mathbf{m}$ to yield

$$\mathbf{m} = \hat{\mathbf{m}} + \left[\mathbf{J}^T\mathbf{G}^T\mathbf{GJ} + \mu\mathbf{H}^T\mathbf{H}\right]^{-1}\left[\mathbf{J}^T\mathbf{G}^T\mathbf{Gd} - \mathbf{J}\hat{\mathbf{m}}\right]. \tag{6.9}$$

The presence of the term $\mu\mathbf{H}^T\mathbf{H}$ within the square brackets in (6.9) ensures that the matrix to be inverted is well conditioned.

The regularization matrix $\mathbf{H}$ in (6.8) and (6.9) provides considerable flexibility in the application of a priori information in the inversion. For instance, if prior model parameter estimates $\hat{\mathbf{m}}$ are available, an appropriate weighting is given by [vS89]:

$$\mathbf{H} = \text{diag}[1/\xi_1, \ldots, 1/\xi_M], \tag{6.10}$$

where ξ_j represents the uncertainty for the jth parameter estimate $\hat{m}_j$. This weighting correctly applies prior parameter estimates which can vary over orders of magnitude in uncertainty. An alternative form of regularization is to apply a priori information to derivatives of the model parameters [C+87], [P+92]. For instance, if the a priori expectation is that the parameters are well approximated by a smooth function, then an appropriate choice is $\hat{\mathbf{m}} = \mathbf{0}$ and

$$\mathbf{H} = \begin{bmatrix} -1 & 2 & -1 & 0 & 0 & 0 & 0 & \cdots & 0 \\ 0 & -1 & 2 & -1 & 0 & 0 & 0 & \cdots & 0 \\ \vdots & & & & \ddots & & & & \vdots \\ 0 & \cdots & 0 & 0 & 0 & -1 & 2 & -1 & 0 \\ 0 & \cdots & 0 & 0 & 0 & 0 & -1 & 2 & -1 \end{bmatrix}. \tag{6.11}$$

For this choice of $\hat{\mathbf{m}}$ and $\mathbf{H}$, $\mathbf{H}(\mathbf{m} - \hat{\mathbf{m}})$ represents a discrete approximation to the second derivative of $\mathbf{m}$, and the regularization term in (6.8) provides a measure of the total curvature or roughness R of the model:

$$R = |\mathbf{H}(\mathbf{m} - \hat{\mathbf{m}})|^2. \tag{6.12}$$

Applying this regularization minimizes the model roughness, producing a minimum-structure solution. In each case, the regularization is appropriately applied by choosing the trade-off parameter μ so that the χ^2 data misfit achieves its expected value of $\langle\chi^2\rangle = N$ for N data [P+92], thereby applying the a priori information subject to ensuring that the data are fit to a statistically appropriate level.

The AEL inverse problem considered here involves both types of a priori information described above. In particular, prior parameter estimates for the source locations are available from the consort ship navigation, and the prior estimate for the sound-speed bias is zero. The expectation that the towed array shape is smooth can be applied by minimizing the three-dimensional curvature (roughness). To simultaneously apply two different types of a priori information to a linear inverse problem, an augmented objective function can be formed which includes two regularization terms [D+98a]:

$$\phi = |\mathbf{G}(\mathbf{Jm} - \mathbf{d})|^2 + \mu_1|\mathbf{H}_1(\mathbf{m} - \hat{\mathbf{m}}_1)|^2 + \mu_2|\mathbf{H}_2(\mathbf{m} - \hat{\mathbf{m}}_2)|^2. \tag{6.13}$$

In (6.13), the first regularization term is taken to represent the a priori parameter estimates for the source locations and sound-speed bias. Hence, $\hat{\mathbf{m}}_1$ consists of the prior estimates for these parameters, with zeros for the remaining parameters. The regularization matrix $\mathbf{H}_1$ is of the form of (6.10) with diagonal elements consisting of the reciprocal of the estimate uncertainty for parameters with prior estimates, and zeros for the remaining parameters. The second regularization term is taken to represent the a priori expectation of a smooth array shape. Hence, $\hat{\mathbf{m}}_2$ is taken to be zero, and $\mathbf{H}_2$ is of the form of (6.11) for the sensor position parameters, with rows of zeros corresponding to the remaining parameters. Rows of zeros are also included in $\mathbf{H}_2$ at appropriate locations to separate the measures of curvature in x, y, and z. In this case, minimizing (6.13) leads to the solution

$$\mathbf{m} = \hat{\mathbf{m}}_1 + \left[\mathbf{J}^T\mathbf{G}^T\mathbf{GJ} + \mu_1\mathbf{H}_1^T\mathbf{H}_1 + \mu_2\mathbf{H}_2^T\mathbf{H}_2\right]^{-1}\left[\mathbf{J}^T\mathbf{G}^T\mathbf{Gd} - \mathbf{J}\hat{\mathbf{m}}_1\right]. \tag{6.14}$$

The AEL inversion algorithm consists of an iterative application of (6.14), initiated from an arbitrary starting model. Convergence of the algorithm is based on two criteria: (i) obtaining a misfit to the measured data of $\chi^2 = N$ for N data; and (ii) obtaining a stable solution such that the rms (root-mean-square) change in the sensor positions between iterations is $\Delta < 0.1$ m. Regarding the first criterion, note that although (6.14) is derived based on the χ^2 misfit for the linear inverse problem (6.5) that approximates the nonlinear problem (6.1) at each iteration, the convergence of the inversion algorithm must be judged in terms of the misfit to the nonlinear problem

$$\chi^2 = |\mathbf{G}(\mathbf{T}(\mathbf{m}) - \mathbf{t})|^2. \tag{6.15}$$

An equivalent, and sometimes more convenient, measure is the rms data misfit

$$X = \left[\chi^2/N\right]^{1/2}, \tag{6.16}$$

with an expected value $\langle X \rangle = 1$.

The most subtle aspect of implementing the inversion has to do with assigning values to the two trade-off parameters, μ_1 and μ_2, which control the balance between the data misfit and the two types of a priori information. An effective procedure [D+98a] is to set

$$\mu_2 = \alpha\mu_1 \tag{6.17}$$

for a fixed value of α, and determine the value of μ_1 at each iteration which yields the desired χ^2 misfit (discussed below). The final model obtained from this procedure can then be examined to ascertain whether the value of α was appropriate based on a comparison of the parameter residuals. This comparison can be quantified by defining the rms misfit associated with the a priori estimates

$$\hat{X} = [|\mathbf{H}_1(\mathbf{m} - \hat{\mathbf{m}}_1)|^2 / \hat{M}]^{1/2}, \tag{6.18}$$

where $\hat{M}$ is the number of model parameters with a priori estimates. To fit the prior estimates within their uncertainties, $\hat{X} \approx 1$. If $\hat{X} \ll 1$, then a smaller value of α is required; if $\hat{X} \gg 1$, a larger value of α is required. The inversion can be repeated with a new value of α until $\hat{X} \lesssim 1$ is achieved. In practice, determining an appropriate value for α is a straightforward procedure, typically requiring only two or three trial inversions. The value for α need not be refined too highly, since the uncertainties of the parameter estimates are only approximate, and the sensor positions recovered in the inversion are not generally sensitive to changes in α of less than about a factor of 2.

The above procedure reduces the problem of determining two trade-off parameters to a one-dimensional search for the parameter μ_1 that produces the desired rms misfit X at each iteration. The trade-off parameter μ_1 is chosen so that X is reduced by approximately a factor of 100 at each iteration until $X = 1$ is achieved. Controlling the change in misfit in this manner limits the change in the model at each iteration. This helps ensure that the linear approximation is valid, and stabilizes the convergence. Since X increases monotonically with μ_1, it is straightforward to determine the value for μ_1 which produces the desired X at a given iteration. At early iterations an approximate value for μ_1 is sufficient, and a bisection algorithm is employed. Near convergence, the bisection solution is improved by applying one or more iterations of Newton's method to determine a precise value for μ_1.

Finally, for a linear inverse problem and Gaussian noise, the marginal a posterior probability distribution for the ith model parameter is also Gaussian, with mean equal to the inversion result and variance given by the ith diagonal entry of the solution covariance matrix

$$\mathbf{C} = \langle (\mathbf{m} - \langle \mathbf{m} \rangle)(\mathbf{m} - \langle \mathbf{m} \rangle)^T \rangle. \tag{6.19}$$

Substituting from (6.14) into (6.19) leads (after some manipulation) to

$$\mathbf{C} = [\mathbf{J}^T \mathbf{G}^T \mathbf{G} \mathbf{J} + \mu_1 \mathbf{H}_1^T \mathbf{H}_1 + \mu_2 \mathbf{H}_2^T \mathbf{H}_2]^{-1}. \tag{6.20}$$

This expression includes the effect of the smoothness regularization (μ_2 term). However, it can be argued that this regularization represents a somewhat arbitrary prior assumption which is difficult to quantify, and that it is preferable to omit this term and define the covariance matrix

$$\mathbf{C} = [\mathbf{J}^T \mathbf{G}^T \mathbf{G} \mathbf{J} + \mu_1 \mathbf{H}_1^T \mathbf{H}_1]^{-1}. \tag{6.21}$$

In practice, it is generally found that (6.20) and (6.21) produce very similar values, although (6.21) always yields slightly larger variances (i.e., is a more conservative

estimate). Finally, the expected standard deviation σ_i of parameter m_i is given by

$$\sigma_i = \sqrt{\mathbf{C}_{ii}}. \tag{6.22}$$

The parameter error estimates σ_i depend on the data uncertainties through $\mathbf{G}$, on the uncertainties in the a priori parameter estimates through $\mathbf{H}_1$, and on the source–receiver geometry through $\mathbf{J}$. The above uncertainty analysis applies to linear inverse problems; however, for linearized inversions such as AEL, it can provide meaningful estimates of the expected uncertainty [DS99]. A particularly useful application of the a posterior uncertainty is in optimal survey design, considered in the following section.

6.2.3 *Optimal Experiment Design*

The previous section developed an inversion algorithm for localizing the sensors of a towed array using sources deployed by two escort ships. This section considers the related problem of determining the optimal survey geometry, i.e., the configuration of source positions that produces the most accurate inversion for sensor positions. To this end, an AEL error measure is defined based on the a posterior uncertainties of the recovered sensor positions from (6.21) and (6.22). The optimal survey configuration can then be determined by minimizing this error measure with respect to the source positions [DS99]. Note that this procedure is based on an *expected* inverse problem (i.e., the array configuration, data errors, and parameter uncertainties are assumed, but there are no data to invert). In this case, an appropriate value of the trade-off parameter μ_1 in (6.21) can be determined by carrying out a number of representative synthetic inversions with randomly generated errors and uncertainties.

A number of different AEL error measures can be defined using the standard deviations of the individual sensor-position parameters given by (6.22). Let σ_x, σ_y, σ_z represent the standard deviations of the x, y, z Cartesian coordinates of the sensor positions and let $\sigma_r = [\sigma_x^2 + \sigma_y^2 + \sigma_z^2]^{1/2}$. The error measure that is considered here is

$$E = \frac{1}{N_S} \sum_r \sigma_r, \tag{6.23}$$

where N_S is the total number of sensors to be localized. This measure represents the mean three-dimensional error of the sensor positions. The source configuration that minimizes this error measure will provide the sensor-position estimates that are the most accurate on average. Alternatively, the maximum sensor-position error can be minimized [DS99]. Other error measures can also be devised and may be appropriate for specific AEL objectives. For example, if accurate sensor depths are deemed more important than accurate horizontal positions, the σ_z term in the definition of σ_r could be weighted by a factor greater than one and E minimized; however, such cases are not considered further here.

Optimal AEL survey design consists of determining the set of source-position parameters that minimizes the sensor-position error E. This is a strongly nonlinear

minimization problem which typically has a large number of local minima, and is not amenable to linear optimization methods. Global optimization methods, such as simulated annealing (SA) [HS94] and genetic algorithms (GA) [HB98], have been applied to minimization problems associated with geophysical experiment design, but can be relatively inefficient. Recently, hybrid optimization methods have been developed and applied to geophysical [L+95] and ocean-acoustic [FD99] inverse problems. Hybrid methods combine local and global approaches to produce a more efficient optimization. Here, a hybrid optimization algorithm that combines the local downhill simplex (DHS) method with SA is applied to optimal AEL survey design. For completeness, the following subsections briefly describe SA, DHS and the hybrid simplex simulated annealing (SSA) algorithms. For more details, see [DS99].

Simulated Annealing (SA)

SA is a global optimization method that can be applied to minimize a function E with respect to a set of model parameters defined on a given search interval. The algorithm consists of a series of iterations involving random perturbations of the parameters. After each iteration a control parameter, the temperature T, is decreased slightly. Perturbations that decrease E are always accepted; perturbations that increase E are accepted conditionally, with a probability P that decreases with T according to the Boltzmann distribution

$$P(\Delta E) = \exp(-\Delta E/T). \tag{6.24}$$

Accepting some perturbations that increase E allows the algorithm to escape from local minima in search of a better solution. As T decreases, however, accepting increases in E becomes increasingly improbable, and the algorithm eventually converges. The rate of reducing T and the number and type of perturbations define the annealing schedule. The method of fast SA (FSA) [SH76] is based on using a Cauchy distribution to generate the parameter perturbations and reducing the width of the distribution with the temperature. The narrow peak and flat tails of the Cauchy distribution provide concentrated local sampling together with occasional large perturbations, allowing a faster rate of temperature reduction than standard SA.

Downhill Simplex (DHS)

Global optimization methods widely search the parameter space and avoid becoming trapped in unfavorable local minima. However, since individual steps are computed randomly, these methods can be quite inefficient at moving downhill. In contrast, local (gradient-based) methods move efficiently downhill, but typically become trapped in a local minimum close to the starting model. The DHS method [P+92] is a local inversion technique based on a geometric scheme for moving downhill in E that does not require the computation of partial derivatives or the solution of systems of equations. DHS navigates the search space using a simplex of $M + 1$ models in an M-dimensional parameter space (e.g., Figure 6.1(a), for

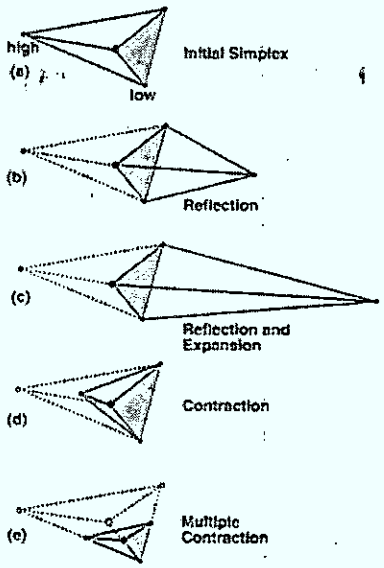

FIGURE 6.1. DHS steps in three dimensions (after [P+92]).

$M = 3$). The algorithm initially attempts to improve the model with the highest value of E by reflecting it through the opposite face of the simplex (Figure 6.1(b)). If the new model has the lowest E in the simplex, an extension by a factor of 2 in the same direction is attempted (Figure 6.1(c)). If the model obtained by the reflection still has the highest E, the reflection is rejected and a contraction by a factor of 2 along this direction is attempted (Figure 6.1(d)). If none of these steps decrease E, then a multiple contraction about the lowest-E model is performed (Figure 6.1(e)). This process is repeated until the value of E for each model of the simplex converges to a common value (i.e., the simplex shrinks to a single point).

Simplex Simulated Annealing (SSA)

The goal of hybrid inversion is to combine local and global methods to exploit the advantages of each (i.e., to move efficiently downhill, yet avoid becoming trapped in local minima). Here, a hybrid SSA inversion is described that incorporates the local DHS method into a global SA search. Unlike standard SA, the SSA inversion operates on a simplex of models rather than on a single model, and instead of employing purely random model perturbations, DHS steps with a random component are applied to perturb the models. To introduce the random component, the DHS steps are not computed directly from the current simplex of models, but rather from a secondary simplex which is formed by applying random perturbations to all the model parameters and E values associated with the current simplex. The perturbations to the current simplex used to produce the secondary simplex are computed using a Cauchy distribution and reducing the distribution width with temperature as follows. Each source-position parameter $u \in \{x, y, z\}$ is perturbed

according to

$$u \leftarrow u + \zeta\delta, \tag{6.25}$$

where δ represents the difference between the upper and lower limits assumed for u and the quantity ζ is a temperature-dependent, Cauchy-distributed random variable computed as

$$\zeta = \left[T_j/T_0\right]^{\frac{1}{2}} \tan\left[\pi\left(\eta - \tfrac{1}{2}\right)\right]. \tag{6.26}$$

In (6.26), η is a uniform random variable on [0, 1], and T_j is the temperature at the jth step. The perturbation to the value of E associated with each model in the simplex is computed according to

$$E \leftarrow E + \zeta\bar{E}, \tag{6.27}$$

where ζ is computed according to (6.26) and $\bar{E}$ is the mean value of E for the current simplex. Each new model proposed by a DHS step is evaluated for acceptance based on the probabilistic criterion of SA applied to the actual (not perturbed) energies, before and after perturbation, for that model. This provides a mechanism for accepting uphill steps and escaping from local minima. If any DHS step results in parameter values outside their given search interval, the parameters are set to the interval bound prior to evaluation. After the set of perturbations is complete, the temperature is reduced according to

$$T_j = \beta^j T_0, \tag{6.28}$$

where β is a constant less than one. An appropriate starting temperature T_0 can be determined by requiring that at least 90% of all perturbations are accepted initially. Appropriate values for β and the number of perturbations per temperature step are usually straightforward to determine with some experimentation.

At high temperatures where the random component of the perturbations dominates, the SSA method resembles an FSA global search. At low temperatures, where the random component is small, the method resembles the local DHS method. At intermediate temperatures, the method makes a smooth transition between these two endpoints. The efficiency of the algorithm can be improved further by "quenching" the optimization when it approaches convergence (i.e., when E effectively stops decreasing) by switching to a pure DHS algorithm to avoid the slow final convergence typical of SA. A block diagram illustrating the basic SSA algorithm is given in Figure 6.2.

6.2.4 *Ray Travel Times and Derivatives*

For completeness, this subsection describes the classical ray theory applied to compute the acoustic travel times and partial derivatives required in the inversion and optimal survey design algorithms of the previous subsections. Consider an acoustic source and receiver in the ocean at (x_j, y_j, z_j) and (x_i, y_i, z_i), respectively, with $z_j < z_i$ (source above receiver is assumed in the equations given here; for

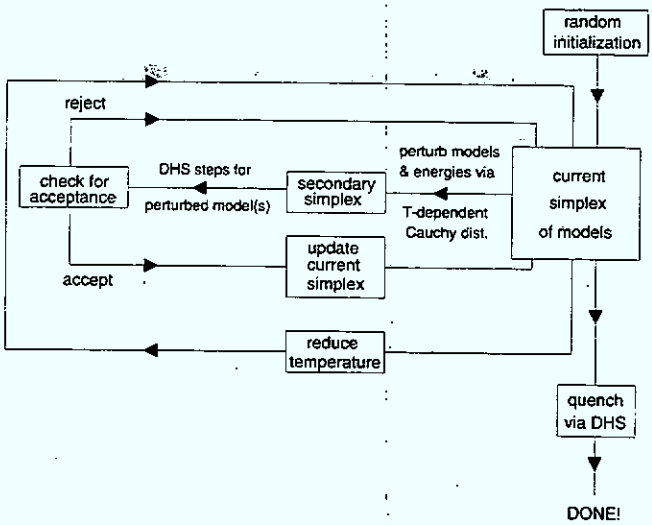

FIGURE 6.2. Block diagram illustrating the SSA algorithm (after [FD99]).

the reverse, a negative sign is required in all integrals unless otherwise noted). The horizontal range between source and receiver is given by

$$r = \sqrt{(x_i - x_j)^2 + (y_i - y_j)^2}. \tag{6.29}$$

Expressions for the range r and arrival time T along a (nonturning) ray path between source and receiver are easily derived by applying Snell's law to an infinite stack of infinitesimal layers [T+76]:

$$r = \int_{z_j}^{z_i} \frac{pc(z)\,dz}{\left[1 - p^2c^2(z)\right]^{1/2}}, \tag{6.30}$$

$$T = t^0 + \int_{z_j}^{z_i} \frac{dz}{c(z)\left[1 - p^2c^2(z)\right]^{1/2}}, \tag{6.31}$$

where t^0 represents the source instant. In (6.30) and (6.31), the ray parameter $p = \cos\theta(z)/c(z)$ is constant along a ray path, and defines the take-off (grazing) angle at the source. The ray parameter for an eigenray connecting source and receiver is usually determined by searching for the value of p which produces the correct range (to a specified tolerance) using (6.30). An efficient procedure of determining p for direct-path eigenrays is based on Newton's method [D+98a]. An initial estimate p_0 is calculated assuming straight-line propagation with a sound speed c_H representing the harmonic mean of the measured sound-speed profile between source and receiver

$$c_H = (z_i - z_j) \Big/ \int_{z_j}^{z_i} \frac{dz}{c(z)} \tag{6.32}$$

(this equation holds for $z_j < z_i$ or $z_i < z_j$). An improved estimate p_1 is obtained by expanding $r(p)$ in a Taylor's series about p_0 and neglecting nonlinear terms to give

$$r(p) = r(p_0) + \frac{\partial r(p_0)}{\partial p}(p_1 - p_0), \tag{6.33}$$

which has a solution

$$p_1 = p_0 + \left[\frac{\partial r(p_0)}{\partial p}\right]^{-1} (r(p) - r(p_0)). \tag{6.34}$$

In (6.34), $\partial r/\partial p$ is determined by differentiating (6.30) to yield

$$\frac{\partial r}{\partial p} = \int_{z_j}^{z_i} \frac{c(z)\,dz}{[1 - p^2c^2(z)]^{3/2}}. \tag{6.35}$$

If $r(p_1)$ computed from (6.30) is within the tolerance of the desired range, the procedure is complete. If not, the starting value is updated, $p_0 \leftarrow p_1$, and the procedure repeated iteratively until a satisfactory value is obtained. The travel time along the ray path is then computed using (6.31). Since Newton's method converges quadratically near the solution, this is an efficient method of determining direct eigenrays to high precision.

In addition to computing travel times, the linearized inversion algorithm requires partial derivatives of travel time with respect to source and receiver coordinates, source instant, and sound-speed bias. Consider first the partial derivative with respect to horizontal coordinate x_i. Employing the chain rule

$$\frac{\partial T}{\partial x_i} = \frac{\partial T}{\partial p}\frac{\partial p}{\partial r}\frac{\partial r}{\partial x_i} = \frac{\partial T}{\partial p}\left[\frac{\partial r}{\partial p}\right]^{-1}\frac{\partial r}{\partial x_i}. \tag{6.36}$$

The three partials on the right side of (6.36) can be calculated from (6.31), (6.30), and (6.29), respectively, yielding

$$\frac{\partial T}{\partial x_i} = p(x_i - x_j)/r. \tag{6.37}$$

Similarly, partial derivatives with respect to the other horizontal coordinates are

$$\frac{\partial T}{\partial x_j} = p(x_j - x_i)/r, \tag{6.38}$$

$$\frac{\partial T}{\partial y_i} = p(y_i - y_j)/r, \tag{6.39}$$

$$\frac{\partial T}{\partial y_j} = p(y_j - y_i)/r. \tag{6.40}$$

The partial derivative of T with respect to vertical coordinate z_i can be determined by differentiating (6.31) to give

$$\frac{\partial T}{\partial z_i} = \int_{z_j}^{z_i} \frac{pc(z)\,dz}{[1 - p^2c^2(z)]^{3/2}}\left(\frac{\partial p}{\partial z_i}\right) - \frac{1}{c(z_i)\left[1 - p^2c^2(z_i)\right]^{1/2}}. \tag{6.41}$$

An expression for $\partial p/\partial z_i$ can be obtained by noting that

$$\frac{\partial r}{\partial z_i} = 0 = \int_{z_j}^{z_i} \frac{c(z)\,dz}{\left[1 - p^2c^2(z)\right]^{3/2}} \left(\frac{\partial p}{\partial z_i}\right) - \frac{pc(z_i)}{\left[1 - p^2c^2(z_i)\right]^{1/2}}. \tag{6.42}$$

Solving for $\partial p/\partial z_i$ and substituting into (6.41) yields

$$\frac{\partial T}{\partial z_i} = \frac{1}{c(z_i)}\left[1 - p^2c^2(z_i)\right]^{1/2}. \tag{6.43}$$

Similarly,

$$\frac{\partial T}{\partial z_j} = -\frac{1}{c(z_j)}\left[1 - p^2c^2(z_j)\right]^{1/2}. \tag{6.44}$$

To account for bias in the measured sound-speed profile, let $c(z) = c_t(z) + c_b$, where $c_t(z)$ is the true sound speed and c_b is the bias. Differentiating (6.31) with respect to c_b (and noting $\partial p/\partial c = -p/c$) leads to

$$\frac{\partial T}{\partial c_b} = -\int_{z_j}^{z_i} \frac{dz}{c^2(z)\left[1 - p^2c^2(z)\right]^{1/2}}. \tag{6.45}$$

Finally, the derivative of T with respect to the source instant t^0 in (6.31) is simply given by

$$\frac{\partial T}{\partial t^0} = 1. \tag{6.46}$$

To implement numerically the equations derived above, it is assumed that a digital sound-speed profile can be represented by a series of layers with a linear sound-speed gradient in each layer. The simplest ray paths to trace involve bottom and/or surface reflections, since these do not involve turning points (i.e., points where the ray passes through zero grazing angle and changes vertical direction as the result of refraction). Sea surface and bottom reflections are modeled using the method of images, i.e., representing the reflected path by adirect ray path from an image source located above the surface or below the bottom, respectively. Ray paths involving both surface and bottom reflections require both an image source and an image receiver. To apply the method of images, the sound-speed profile is reflected about the interfaces in the same manner as the sources. In the following, let $\{(z_k, c_k)\}$ represent the sound-speed profile including the requisite reflections for a particular reflected path, let $\{c_k'\}$ be the corresponding sound speed gradients, and let z_j and z_i be the source and receiver depths, respectively. For the case of linear sound-speed gradients, the integrals in equations (6.30), (6.31), (6.35), and (6.45) can be evaluated analytically, yielding the following results, where $w_k \equiv (1 - p^2c_k^2)^{1/2}$:

$$r = \sum_{k=j}^{i-1} \frac{w_k - w_{k+1}}{pc_k'}, \tag{6.47}$$

$$T = t^0 + \sum_{k=j}^{i-1} \frac{1}{c'_k} \left[\log_e \frac{c_{k+1}(1+w_k)}{c_k(1+w_{k+1})} \right], \tag{6.48}$$

$$\frac{\partial r}{\partial p} = \sum_{k=j}^{i-1} \frac{w_k - w_{k+1}}{p^2 c'_k w_k w_{k+1}}, \tag{6.49}$$

$$\frac{\partial T}{\partial c_b} = \sum_{k=j}^{i-1} \frac{1}{c'_k} \left[\frac{w_{k+1}}{c_{k+1}} - \frac{w_k}{c_k} \right]. \tag{6.50}$$

Calculating integrals along direct ray paths is somewhat more complicated, since these paths can involve turning rays. Rather than simply integrating (summing) along the ray path from source to receiver as per the reflected rays above, the possibility that the direct ray turns must be checked as it enters each layer along its path. Consider the case of a downward-propagating ray entering the kth layer. The turning depth for this ray is given by

$$z_T = z_k + (1/p - c_k)/c'_k. \tag{6.51}$$

If this depth is less than z_{k+1} (the bottom of the kth layer) the ray turns; if not, it proceeds into layer $k+1$. If the direct ray does not turn between source and receiver, (6.47)–(6.50) apply. However, if the direct ray turns in layer t, then the correct procedure involves four steps:

(i) integrate from the source depth z_j down to z_t (the top of the tth layer) using the above equations;

(ii) integrate from z_t to the turning depth z_T (where, by definition, $w_T = 0$);

(iii) integrate upward from z_T to z_t; and

(iv) integrate upward from z_t to the receiver depth z_i. Applying this procedure leads to the following equations for turning rays:

$$r = \sum_{k=j}^{t-1} \frac{w_k - w_{k+1}}{pc'_k} + \frac{2w_t}{pc'_t} + \sum_{k=t}^{i+1} \frac{w_k - w_{k-1}}{pc'_{k-1}}, \tag{6.52}$$

$$T = t^0 + \sum_{k=j}^{t-1} \frac{1}{c'_k} \left[\log_e \frac{c_{k+1}(1+w_k)}{c_k(1+w_{k+1})} \right] + \frac{2}{c'_t} \log_e \frac{1+w_t}{pc_t} + \sum_{k=t}^{i+1} \frac{1}{c'_{k-1}} \left[\log_e \frac{c_{k-1}(1+w_k)}{c_k(1+w_{k-1})} \right], \tag{6.53}$$

$$\frac{\partial r}{\partial p} = \sum_{k=j}^{t-1} \frac{w_k - w_{k+1}}{p^2 c'_k w_k w_{k+1}} - \frac{2}{c'_t p^2 w_t} + \sum_{k=t}^{i+1} \frac{w_k - w_{k-1}}{p^2 c'_{k-1} w_k w_{k-1}}, \tag{6.54}$$

$$\frac{\partial T}{\partial c_b} = \sum_{k=j}^{t-1} \frac{1}{c'_k} \left[\frac{w_{k+1}}{c_{k+1}} - \frac{w_k}{c_k} \right] + \frac{2w_t}{c_t c'_t} + \sum_{k=t}^{i+1} \frac{1}{c'_{k-1}} \left[\frac{w_{k-1}}{c_{k-1}} - \frac{w_k}{c_k} \right]. \tag{6.55}$$

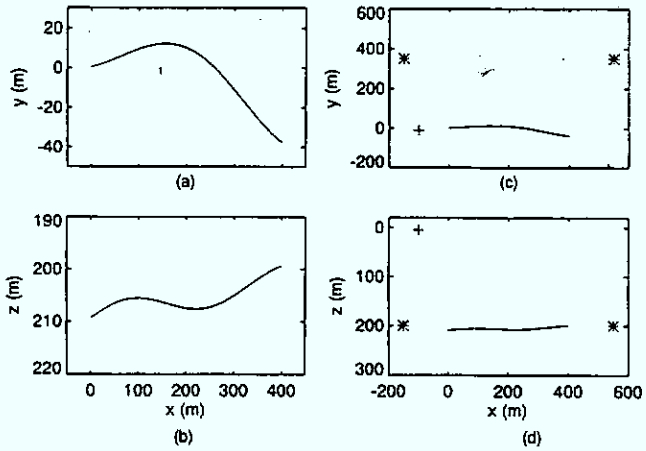

FIGURE 6.3. Source-receiver geometry for the synthetic examples. (a) and (b) show the towed array in x–y and x–z planes, respectively. (c) and (d) show the same at a larger scale, and include the positions of the sources (asterisks) and the ship-mounted reference hydrophone (cross).

6.3 Examples

6.3.1 Inversion for Towed-Array Shape

This subsection illustrates the regularized inversion algorithm for towed-array shape estimation with a number of synthetic examples. Figure 6.3 shows the source–receiver geometry for the examples. The array consists of 41 sensors, each nominally separated by 10 m, for a total array length of approximately 400 m. The array is curved in the horizontal (x–y) plane, as shown in Figure 6.3(a), representing the effect of a course change by the tow ship (assumed to be to the left of the array, see Figure 6.3(c)). The total horizontal deflection of the array is approximately 40 m. The array tilts generally upward (from fore to aft) in the vertical (x–z) plane with a slight undulation near the center of the array, as shown in Figure 6.3(b). The sensor depths vary from 200–210 m. The two acoustic sources are located at 500 m range from the center of the array, and are separated by 90° with respect the array; the source depth is 200 m (Figure 6.3(c) and (d)). The source positions are assumed to be known in x and y to within ± 10 m, representing the approximate accuracy that could be obtained using DGPS (differential global positioning system) locations for the consort ships. The uncertainty in source depth is 2 m, consistent with the experiment described in [vB+89]. The reference hydrophone (mounted on the tow ship) is located 100 m to the left of the array (Figure 6.3(c)). The ocean is 4000 m deep with a typical N.E. Pacific sound-speed profile, shown in Figure 6.4.

The measured (synthetic) data consist of relative travel times along direct, bottom reflected, and bottom–surface reflected paths. The data were computed using the ray-tracing algorithm outlined in Section 6.2.4, and subsequently adding random (Gaussian) errors. Several different levels of error (standard deviation) are

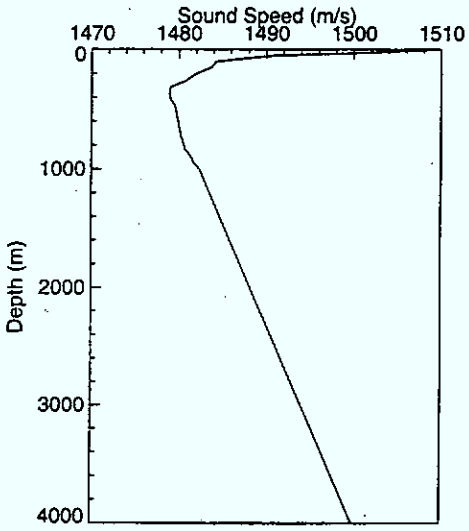

FIGURE 6.4. Ocean sound-speed profile for synthetic examples.

considered. In particular, the errors for the direct-path travel times are either 0.2, 0.5, or 1 ms. In each case, the errors for the bottom-reflected arrivals are twice as large as those on the direct arrivals, while the errors on the bottom-surface reflected arrivals are three times as large. The use of larger errors for reflected arrivals is designed to represent two factors that affect actual data measurements and inversion:

(i) the resolution in picking arrival times is generally lower for reflected paths due to the loss of high-frequency energy; and

(ii) modeling errors are larger for reflected arrivals due to the fact that the sea floor and surface are not completely flat and smooth.

In addition, the prior estimates for the source locations used in the inversion included Gaussian errors with standard deviations of 10 m for the x- and y-coordinates and 2 m for the z-coordinate. Finally, a sound-speed bias of standard deviation 2 m/s was included in the sound-speed profile used in the inversion.

Figures 6.5 and 6.6 illustrate the convergence properties of the inversion algorithm for data with an uncertainty of 0.2 ms (direct arrivals). Figure 6.5 shows the convergence in terms of the rms data misfit X, the rms change in sensor positions between iterations Δ, the rms misfit to the prior parameter estimates $\hat{X}$, and the array roughness R. The starting model (iteration 0) consists of a straight array (see Figure 6.6(a)) with the source positions corresponding to the prior estimates. Figure 6.5(a) shows that the data misfit X decreases by more than three orders of magnitude over the first two iterations, then remains constant at the desired value of $X = 1$ for iterations 3 and 4 while the rms change decreases below the threshold of $\Delta = 0.1$ m for convergence (Figure 6.5(b)). The rms prior misfit increases over the first two iterations from $\hat{X} = 0$ at the starting model to a value of 0.85

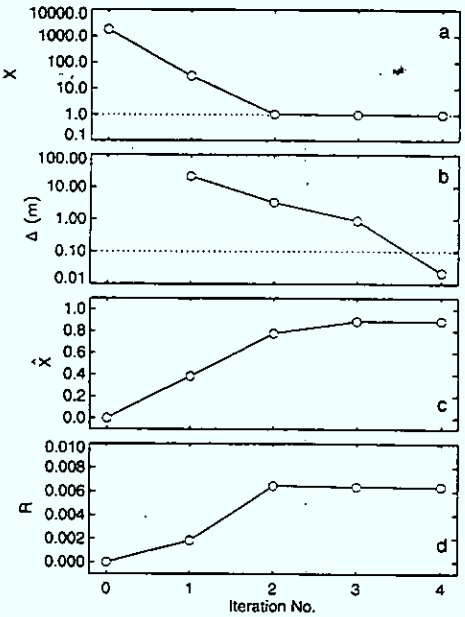

FIGURE 6.5. Convergence properties of the regularized inversion algorithm: (a) rms data misfit X; (b) rms sensor-position change between iterations Δ; (c) rms prior misfit $\hat{X}$; and (d) array roughness R.

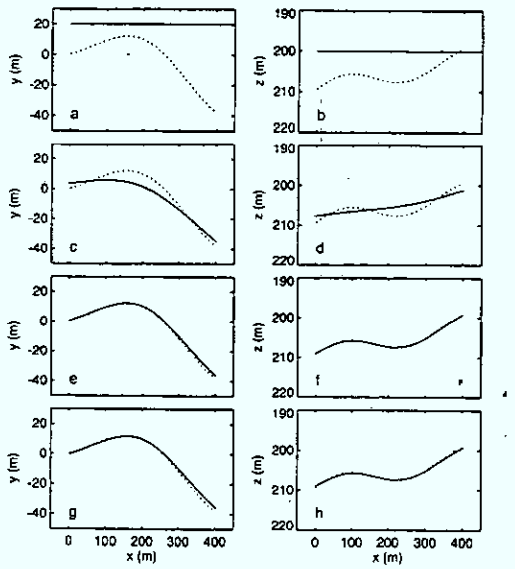

FIGURE 6.6. Towed-array shape at various iterations of the inversion: (a) and (b) show the starting model; (c) and (d) show iteration 1; (e) and (f) show iteration 2; and (g) and (h) show iteration 4 (final model). Dotted lines indicate the true array shape.

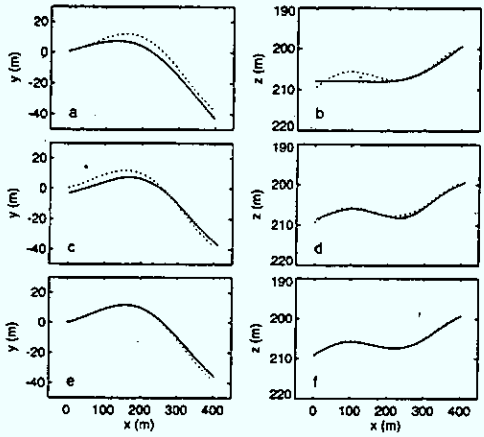

FIGURE 6.7. Towed-array shape estimates from regularized inversion for different error levels: (a) and (b) 1 ms; (b) and (c) 0.5 ms; and (d) and (e) 0.2 ms.

(Figure 6.5(c)), which approximates the expected value of unity. Similarly, the array-shape roughness R increases from an initial zero value to a stable final value. Figure 6.6 shows the array shape at various iterations of the inversion: it is apparent that the inversion algorithm introduces structure into the solution in a controlled manner. The final solution, shown in Figure 6.6(g) and (h), is an excellent estimate of the true array shape but, notably, exhibits slightly less overall curvature than the true shape.

Figure 6.7 illustrates the results of inverting datasets with differing error levels. Figure 6.7(a) and (b) shows the inversion result for data with an uncertainty of 1 ms (direct arrivals). The estimated array shape is a reasonably good approximation of the true shape, although it is noticeably smoother due to the limited resolving power of the noisy data. Note, in particular, that despite relatively large errors on the data, the solution exhibits no spurious structure, but rather represents a conservative estimate of the array shape, exhibiting the minimum structure required to fit the data. Figure 6.7(c) and (d) and Figure 6.7(e) and (f) show the array shapes estimated by inverting data with errors of 0.5 ms and 0.2 ms, respectively. As the data errors decrease, the estimated array shape more closely agrees with the true array shape. However, in each case the solution exhibits slightly less structure (curvature) than the true array.

To illustrate the advantages of the regularized inversion algorithm, the test cases shown in Figure 6.7 are repeated in Figure 6.8 applying a standard least-squares inversion algorithm that minimizes the data misfit and treats source positions as known parameters. Figure 6.8(a) and (b) shows that for data errors of 1 ms, the least-squares solution is substantially rougher than the minimum-structure result of Figure 6.7(a) and (b), with spurious fluctuations of up to 5 m in x and y, and up to 3 m in z. The fluctuations result from the tendency of a least-squares approach to over-fit the data, in effect fitting the noise as well as the data. In addition, the array-shape estimates in Figure 6.8 exhibit greater offsets from the true positions as a

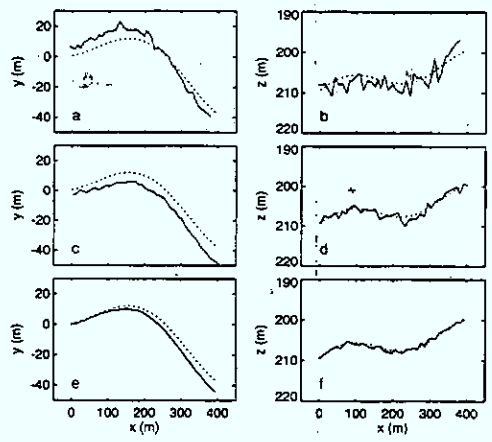

FIGURE 6.8. Towed-array shape estimates from least-squares inversion for different error levels: (a) and (b) 1 ms; (c) and (d) 0.5 ms; and (e) and (f) 0.2 ms.

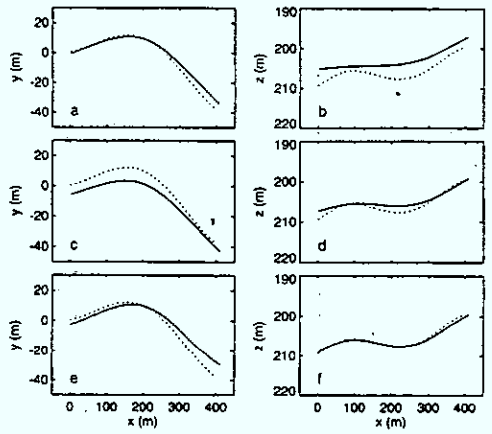

FIGURE 6.9. Towed-array shape estimates from regularized inversion using only direct and bottom-reflected paths for different error levels: (a) and (b) 1 ms; (c) and (d) 0.5 ms; and (e) and (f) 0.2 ms.

result of treating (erroneous) source positions as known parameters. Figure 6.8(c)–(f) show that the magnitude of the fluctuations decrease as the data errors decrease; however, the least-squares results remain significantly poorer than those of the regularized inversion.

The advantages of the regularized inversion are accentuated in cases where travel-time measurements are not available along all three ray paths. To illustrate this, Figures 6.9 and 6.10 show the regularized and least-squares results for the same data errors as in Figures 6.7 and 6.8; however, the inversion is applied to only the direct and bottom-reflected acoustic arrivals (i.e., the datasets do not include the bottom–surface reflected arrivals).

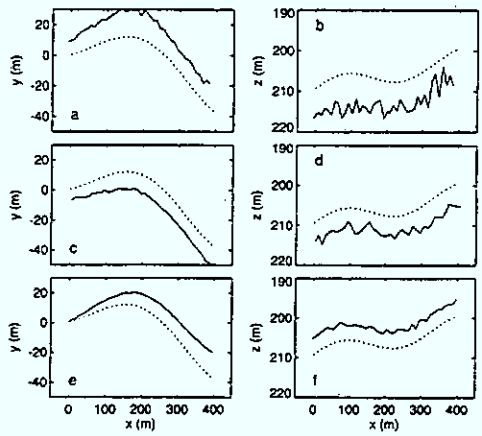

FIGURE 6.10. Towed-array shape estimates from least-squares inversion using only direct and bottom-reflected paths for different error levels: (a) and (b) 1 ms; (c) and (d) 0.5 ms; and (e) and (f) 0.2 ms.

Comparing Figure 6.9 to Figure 6.7 (regularized inversion with complete data), it is apparent that the effect of incomplete data on the regularized inversion is that the solution simply becomes smoother, reflecting the decreased ability of the dataset to resolve the array structure. However, Figure 6.10 shows that the least-squares solution fares considerably worse with incomplete data, exhibiting substantial spurious fluctuations and large offsets from the true solution. Even poorer results (not shown) were obtained for the least-squares inversion when the bottom-reflected arrivals (rather than the bottom–surface reflected arrivals) were omitted.

6.3.2 *Optimal Source Configuration*

In this subsection, the AEL error measure and optimization procedures developed in Section 6.2.3 are applied to investigate the effects of source geometry on towed-array shape estimation using the dual-shot method. The test case considered here is similar to that in Section 6.3.1, with a 400 m array towed at 200 m depth in 4000 m of water. However, since the optimization procedure is designed for a representative (expected) inverse problem, a straight array is assumed here. The data errors are 0.2 ms for the direct arrivals, 0.4 ms for bottom-reflected arrivals, and 0.6 ms for bottom–surface reflected arrivals. The source positions are assumed to be known to within 10 m in x and y and 2 m in z, and the potential sound-speed bias has a standard deviation of 2 m/s. A number of randomly generated trial inversions indicated that a trade-off parameter of $\mu_1 = 10$ is appropriate for this problem. The SSA algorithm described in Section 6.2.3 is applied to determine the source positions (relative to the array) that minimize the mean sensor-position error E given by (6.23).

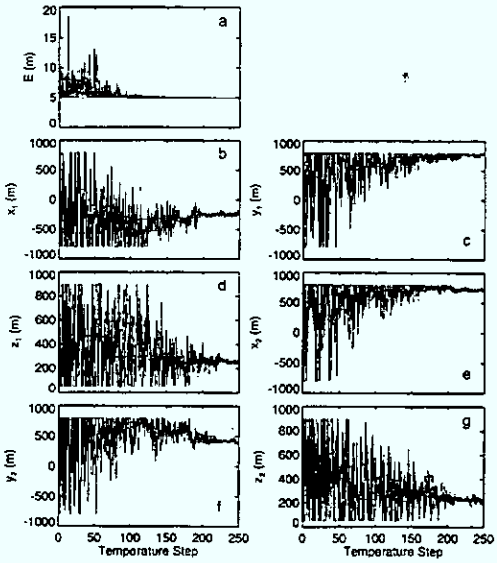

FIGURE 6.11. Convergence of the SSA optimization for source geometry: (a) shows the mean sensor-position error E; and (b)–(g) show the source coordinates $\{x_j, y_j, z_j,\ j = 1, 2\}$.

The convergence of the optimization procedure is illustrated in Figure 6.11, which shows the mean sensor-position error E and the source coordinates $\{x_j, y_j, z_j, j = 1, 2\}$ as a function of temperature step (all models in the simplex are shown). The search limits were set to be $(-800, 800)$ m for x and y, and $(100, 900)$ m for z. The annealing schedule for the optimizations was based on the requirement that ten model perturbations be accepted at each temperature step, with the temperature reduced by a factor of $\beta = 0.95$ between steps. Figure 6.11 shows that initially the source coordinates fluctuate over their entire allowed range, and sensor-position errors as large as $E = 19$ m are obtained. As the temperature is reduced, the error decreases steadily (although not monotonically), and the source coordinates gradually converge to fixed values. By temperature step 250, the error has essentially stopped decreasing, indicating that the various models in the simplex are simply fluctuating between good solutions. The optimization is then quenched to collapse the simplex to the single best model. The sensor-position error for the final solution is $E = 4.95$ m.

The optimal sensor configuration obtained by the SSA algorithm is shown in Figure 6.12. Figure 6.12(a) shows the source positions in the x–y plane; dotted lines indicating a 90° angle with respect to the array center are included as a reference. Note that, unlike the survey geometry suggested in [vB+89], the two sources are not equidistant from the array, and do not fall on the 90° lines. Figure 6.12(b) shows the source positions in the x–z plane. The sources are located at different depths, slightly deeper than the array. The optimal configuration in Figure 6.12 appears to be unique: repeating the SSA optimizations with different sequences, of random

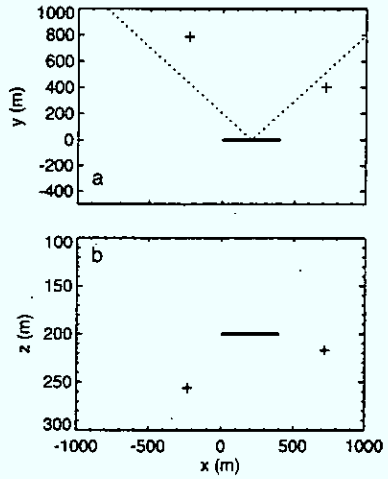

FIGURE 6.12. Optimal source positions (crosses) in: (a) the x–y plane; and (b) the x–z plane. The heavy line indicates the array position, and the dotted lines in (a) indicate a 90° angle with respect to the array center.

model perturbations produced configurations that were essentially identical to that shown, up to reflections about the x- and/or y-axes. However, Figure 6.11 indicates that in the course of the optimization, many different configurations were obtained that were *almost* as good as the optimal configuration. Therefore, it is interesting to compare the optimal configuration to the source geometry suggested in [vB+89] (sources at the same depth as array, equidistant from the array and separated by 90°). To this end, Figure 6.13 shows the mean sensor-position error E computed for the suggested configuration as a function of the range r from the sources to the array center. The error has a minimum of $E = 5.13$ m at a range $r = 339$ m. At shorter ranges, the error increases rapidly; at longer ranges, E increases gradually. The error $E = 4.95$ m obtained for the optimal configuration is included as a dotted line in Figure 6.13. It is apparent that the difference in the sensor-position error that results from using the optimal configuration or the suggested configuration

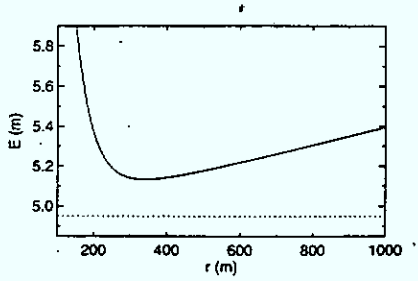

FIGURE 6.13. Mean sensor-position error E for the sources at the same depth as array, equidistant from the array and separated by 90° as a function of the range r from the sources to the array center. The dotted line indicates the error for the optimal configuration.

is small (for a good choice of r). In practice, the source geometry suggested in [vB+89] would seem to be an excellent choice.

6.4 Summary

This chapter considered the inverse problem of estimating the shape of a towed hydrophone array using the relative travel times of direct and reflected acoustic arrivals from sources deployed by a pair of consort ships (the dual-shot method). An algorithm was developed to invert dual-shot data for the most meaningful array-shape estimate. To date, this inversion has been solved as a least-squares problem (minimizing the squared data error), assuming straightline acoustic propagation and neglecting the inevitable errors in the source positions. The new approach is based on an iterated linearized inversion of the ray-tracing equations, which is solved using the method of regularization. The three-dimensional positions of both sources and sensors are treated as unknowns, subject to a priori information. For the sources, the prior information consists of position estimates and uncertainties. For the sensors, the prior information is that the array shape is expected to be smooth: this is applied by minimizing the three-dimensional curvature of the array to obtain a minimum-structure solution. The regularized inversion provides smooth solutions without the spurious fluctuations present in the least-squares solution. Fluctuations in the least-squares solution result from the tendency of a minimum-misfit approach to over-fit the data, in effect fitting the noise as well as the data. The regularized inversion avoids this by trading off data misfits with physical a priori information. In addition, treating source positions as (constrained) unknowns reduces offset-errors in the solution, particularly in cases when not all acoustic arrivals can be used in the inversion.

Finally, the effect of the survey geometry was investigated by quantifying the sensor-position error using the a posterior uncertainty of the inversion. The optimal source configuration was determined by minimizing the sensor-position error with respect to the source positions using an efficient hybrid optimization algorithm. It was found that the standard source configuration typically employed for the dual-shot method, although nonoptimal, provides a good, practical approach to the acoustic survey.

Acknowledgment. This work was supported by a research contract with the Defence Research Establishment Atlantic, Dartmouth, NS, Canada.

6.5 References

[B+96] G.H. Brooke, S.J. Kilistoff, and B.J. Sotirin. Array element localization algorithms for vertical line arrays, in J.S. Papadakis (ed.), *Proceedings of*

the Third European Conference on Underwater Acoustics, pp. 537–542, Crete University Press, 1996.

[C+87] S.C. Constable, R.L. Parker, and C.G. Constable. Occam's inversion: A practical algorithm for generating smooth models from electromagnetic sounding data, *Geophysics*, **52**:289–300, 1987.

[CD82] K.C. Creager and L.M. Dorman. Location of instruments on the seafloor by joint adjustment of instrument and ship positions, *J. Geophys. Res.*, **87**:8379–8388, 1982.

[D+98a] S.E. Dosso, M.R. Fallat, B.J. Sotirin, and J.L. Newton. Array element localization for horizontal arrays via Occam's inversion, *J. Acoust. Soc. Am.*, **104**:846–859, 1998.

[D+98b] S.E. Dosso, G.H. Brooke, S.J. Kilistoff, B.J. Sotirin, V.K. Mcdonald, M.R. Fallat and N.E. Collison. High-precision array element localization of vertical line arrays in the Arctic Ocean", *IEEE J. Ocean. Eng.*, **23**:365–379, 1998.

[DS99] S.E. Dosso and B.J. Sotirin. Optimal array element localization, *J. Acoust. Soc. Am.*, **106**:3445–3459, 1999.

[FD99] M.R. Fallat and S.E. Dosso, Geoacoustic inversion via local, global and hybrid algorithms, *J. Acoust. Soc. Am.*, **105**:3219–3230, 1999.

[HB98] M. Hansruedi and D.E. Boerner. Optimized and robust experimental design: a non-linear application of EM sounding, *Geophys. J. Int.*, **132**:458–468, 1998.

[HS94] M. Hardt and F. Scherbaum. Design of optimum networks for aftershock recording, *Geophys. J. Int.*, **117**:716–726, 1994.

[H+96] W.S. Hodgkiss, D.E. Ensberg, J.J. Murray, G.L. D'Spain, N.O. Booth, and P.W. Schey. Direct measurement and matched-field inversion approaches to array shape estimation, *IEEE J. Ocean. Eng.*, **21**:393–401, 1996.

[LT84] L.R. Lines and S. Treitel. Tutorial: A review of least-squares inversion and its application to geophysical inverse problems, *Geophys. Prosp.*, **32**:159–186, 1984.

[L+95] P. Liu, S. Hartzell, and W. Stephenson. Non-linear multiparameter inversion using a hybrid global search algorithm: Applications in reflection seismology, **Geophys. J. Int.**, **122**:991–1000, 1995.

[Mil83] P.H. Milne. *Underwater Acoustic Positioning Systems*. Cambridge University Press, Cambridge, 1983

[Old83] D.W. Oldenburg. Funnel functions in linear and nonlinear appraisal, *J. Geophys. Res.*: **88**:7387–7398, 1983.

[OC97] J.C. Osler and D.M.F. Chapman. Seismo-acoustic determination of the shear-wave speed of surficial clay and silt sediments on the Scotian shelf, *Canad. Acoust.*, **24**:11–22, 1997.

[P+92] W.H. Press, S.A. Teukolsky, W.T. Vetterling, and B.P. Flannery. *Numerical Recipes in FORTRAN*. Cambridge University Press, Cambridge, 1992.

[S+90] J.A. Scales, P. Docherty, and A. Gersztenkorn. Regularisation of nonlinear inverse problems: Imaging the near-surface weathering layer, *Inverse Problems*, **6**:115–131, 1990.

[SH90] B.J. Sotirin and J.A. Hildebrand. Acoustic navigation of a large-aperture array, *J. Acoust. Soc. Am.*, **87**:154–167, 1990.

[Ste76] B.D. Steinberg. *Principles of Aperture and Array System Design*. Wiley, New York, 1976.

[SH76] H. Szu and R. Hartley. Fast simulated annealing, *Phys. Lett. A.*, **122**:157–162, 1987.

[T+76] W.M. Telford, L.P. Geldart, R.E. Sherif, and D.A. Keys. *Applied Geophysics*. Cambridge University Press, Cambridge, 1976.

[vB+89] E.C. van Ballegooijen, G.W.M. van Mierlo, C. van Schooneveld, P.P.M. van der Zalm, A.T. Parsons, and N.H. Field. Measurement of towed array position, shape and attitude, *IEEE J. Ocean. Eng.*, **14**:375–383, 1989.

[vS89] C. van Schooneveld. Inverse problems: A tutorial survey. In Y.T. Chan (ed.), *Underwater Acoustic Data Processing*, pp. 393–411, Kluwer Academic, Amsterdam, 1989.

[VH98] H.T. Vincent II and S.-L.J. Hu. Geodetic position estimation of underwater acoustic sensors. *J. Acoust. Soc. Am.*, **102**:3099, 1998.